CONDENSED MATTER PHYSICS

10.1126/sciadv.1500797

Tuning bad metal and non-Fermi liquid behavior in a Mott material: Rare-earth nickelate thin films

Evgeny Mikheev, Adam J. Hauser, Burak Himmetoglu, Nelson E. Moreno, Anderson Janotti, Chris G. Van de Walle, Susanne Stemmer*

Resistances that exceed the Mott-Ioffe-Regel limit (known as bad metal behavior) and non-Fermi liquid behavior are ubiquitous features of the normal state of many strongly correlated materials. We establish the conditions that lead to bad metal and non-Fermi liquid phases in $NdNiO_3$, which exhibits a prototype bandwidth-controlled metal-insulator transition. We show that resistance saturation is determined by the magnitude of Ni e_g orbital splitting, which can be tuned by strain in epitaxial films, causing the appearance of bad metal behavior under certain conditions. The results shed light on the nature of a crossover to a non-Fermi liquid metal phase and provide a predictive criterion for Anderson localization. They elucidate a seemingly complex phase behavior as a function of film strain and confinement and provide guidelines for orbital engineering and novel devices.

INTRODUCTION

Mott metal-insulator transitions (MITs) are key to some of the most fascinating topics in materials physics, such as the pathways from a doped Mott insulator to a high-temperature superconductor (*1*) and the feasibility of electronic devices that utilize switchable MITs. Rare-earth nickelates ($RNiO_3$, where R = trivalent rare-earth ion) exhibit a prototype bandwidth-controlled MIT (*2*, *3*). $RNiO_3$ films have recently attracted renewed interest resulting from a prediction that orbital engineering can promote a Fermi surface that resembles that of the cuprate high-temperature superconductors (*4*, *5*). Furthermore, recent discoveries in $RNiO_3$ films point to strikingly similar physics as found in unconventional superconductors. Non-Fermi liquid (NFL) behavior (*6*) and pseudogap phases (*7*) indicate a continuous bandwidth-driven quantum phase transition between a paramagnetic metal and an antiferromagnetic insulator. The $RNiO_3$ family has also been discussed as a new class of "bad metals" (*8*) in the sense that their resistivity escalates above the semiclassical Mott-Ioffe-Regel limit and does not saturate at high temperatures (*9*). Bad metal behavior and NFLs are essential yet poorly understood features of the phase diagrams of unconventional superconductors (*10*). However, neither bad metals nor their counterparts (metals that exhibit resistance saturation) are understood; in both cases, materials enter a regime where classical Boltzmann theory should no longer apply (*11*–*14*).

In this work, we show that rare-earth nickelates are not bad metals: accounting for resistivity saturation is key to correctly describing their electrical transport behavior. The resistivity saturation limit is, however, highly sensitive to the degree of e_g orbital polarization, leading to resistances that exceed the semiclassical Mott-Ioffe-Regel limit. Furthermore, accounting for saturation clarifies many aspects of the strain–film thickness phase behavior and the quantum critical point in the $RNiO_3$ system. In particular, an abrupt crossover between classical Landau Fermi liquid (LFL) and NFL metallic regimes occurs with the suppression of temperature-driven MIT. The metallic phase is an LFL in all cases where a robust MIT is present. We also clarify the conditions leading to Anderson localization in this system, namely, a second disorder-driven MIT: it appears when the resistivity at 0 K approaches the saturation resistance. We develop phase diagrams that can serve as practical guidelines for stabilizing robust MITs in ultrathin nickelate films and that identify new opportunities for control of MITs in general.

Materials Department, University of California, Santa Barbara, CA 93106–5050, USA.
*Corresponding author. E-mail: stemmer@mrl.ucsb.edu

RESULTS

$NdNiO_3$ thin films with thicknesses ranging between 4 and 15 unit cells (u.c.) were grown on substrates chosen to obtain a wide range of epitaxial strains (in parentheses): $YAlO_3$ (−3.58%), $LaAlO_3$ (−1.20%), $NdGaO_3$ (+0.86%), $(LaAlO_3)_{0.3}(Sr_2AlTaO_6)_{0.7}$ (+0.93%), $SrTiO_3$ (+1.72%), and $DyScO_3$ (+2.96%). Figure 1 shows their electrical resistivities as a function of temperature. Several different types of behavior can be discerned, including temperature-driven MITs and films that are metallic or insulating at all temperatures.

We first focus on describing the metallic states. Nickelates are often understood to be NFLs (*6*, *15*–*19*) for which the temperature dependence (T) of resistivity follows a power law with an exponent $n < 2$

$$\rho_{NFL}(T) = \rho_0 + AT^n \quad (1)$$

where ρ_0 is the residual resistivity and A is a measure of the strength of electron-electron scattering. For a LFL, $n = 2$. However, Eq. 1 often describes experimental data only in a limited temperature range (*20*). As will be shown here, the temperature dependence of resistivity in the metallic phase is completely described when we account for resistivity saturation (ρ_{SAT})

$$\rho^{-1}(T) = \rho_{NFL}^{-1}(T) + \rho_{SAT}^{-1} \quad (2)$$

Equation 2, in which ρ_{SAT} acts as a parallel resistor, is known to apply to a wide range of materials that show resistance saturation, including elemental metals, alloys, and heavy fermion compounds (*10*, *21*–*26*). The origins of resistivity saturation and the parallel resistor formula remain subjects of significant debate (*10*–*12*, *21*, *27*–*31*). ρ_{SAT} is often linked to high resistances that approach the Mott-Ioffe-Regel limit (ρ_{MIR}) (*28*),

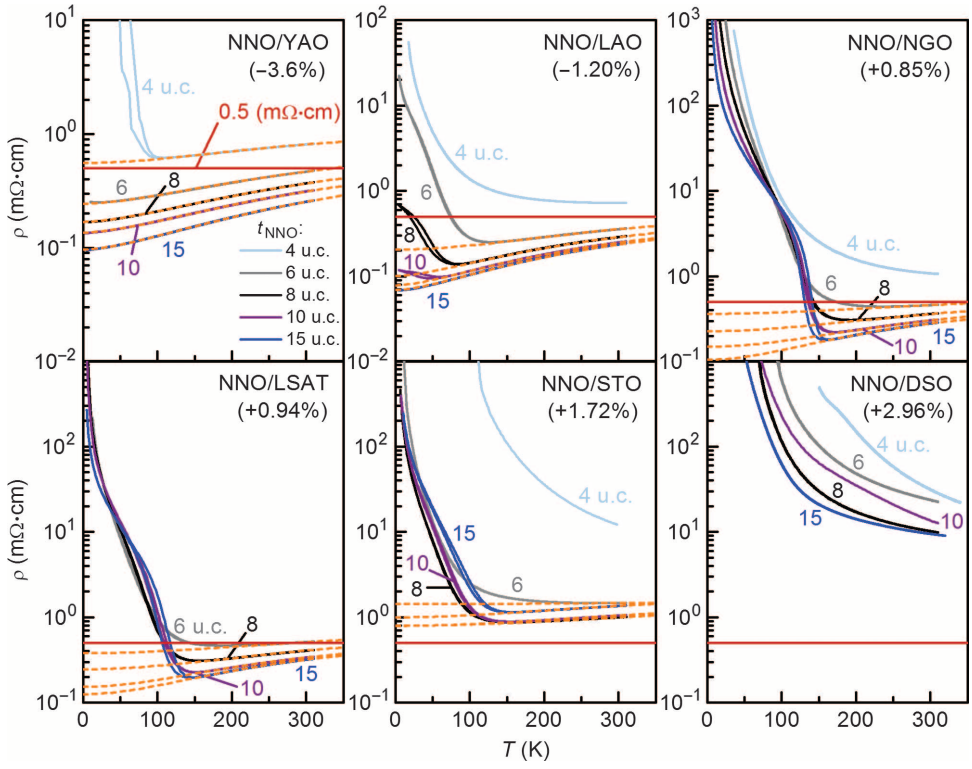

Fig. 1. MITs and temperature dependence of resistivity. The graphs show the resistivity as a function of temperature for $NdNiO_3$ (NNO) films with thicknesses ranging between 4 and 15 u.c. on six different substrates [YAO, $YAlO_3$; LAO, $LaAlO_3$; NGO, $NdGaO_3$; LSAT, $(LaAlO_3)_{0.3}(Sr_2AlTaO_6)_{0.7}$; STO, $SrTiO_3$; DSO, $DyScO_3$]. Each panel corresponds to a different substrate, with the corresponding epitaxial strain noted in parentheses. Solid lines are experimental data and dashed lines are fits using Eqs. 1 and 2. The horizontal solid line is the Mott-Ioffe-Regel limit according to Eq. 3.

which is the semiclassical upper bound for coherent transport in a metal when the carrier mean free path l approaches the interatomic spacing a

$$\rho_{MIR} = \frac{3\pi^2\hbar}{q^2k_F^2a} \quad (3)$$

where $\hbar$ is the reduced Planck constant, q is the elementary charge, and k_F is the Fermi wave vector. For many materials, ρ_{MIR} estimated from Eq. 3 is similar to the observed ρ_{SAT} (*10*). Suggestions as to why ρ_{SAT} acts as a parallel resistor according to Eq. 2 include semiclassical pictures that invoke the existence of a minimum scattering time (*10*, *28*) as well as interband scattering (*29*) that acts as a new conducting channel (*12*, *29*). As has also been pointed out in the literature (*11*, *12*, *32*), it is questionable to use semiclassical arguments in a regime where l is not a well-defined quantity anymore. Quantum Monte Carlo and dynamical mean field theory calculations indicate that resistances can easily exceed the ρ_{MIR} value calculated from Eq. 3 for certain materials (*13*, *14*). In particular, certain materials (including some unconventional superconductors) (*27*) are characterized by saturation at values much higher than the ρ_{MIR} value calculated from Eq. 3, or even a nonsaturating ρ, and these materials have become known as bad metals (*9*).

For $NdNiO_3$ films, Eq. 2 is remarkably successful in describing the metallic state. This can be seen from the dashed lines in Fig. 1, which are fits to Eq. 2. The saturation behavior is also directly seen in the experimental data when plotted as $d\rho/dT$ as a function of T (Fig. 2A). The key feature is the downturn in $d\rho/dT$ at high T (*23*, *26*). This translates to a sublinear scaling of ρ with T, which is due to the increasing contribution from ρ_{SAT}, as expected from Eq. 2. Equation 2 describes the entire metallic state with a single T-independent exponent n (inset to Fig. 2A). Additional examples, including those for $LaNiO_3$ films, are shown in figs. S1 to S3.

When the exponent n was an adjustable parameter in the fits, only two values were obtained across the entire sample set (Fig. 2B): for all films displaying a robust temperature-driven MIT, $n = 2$, indicating a classical LFL. For films that are metallic at all temperatures (MIT completely suppressed) and for some films with a weak MIT at very low T, $n \approx 5/3$, indicating an NFL regime. For example, on $YAlO_3$, all but the 4-u.c. film are metallic at all temperatures and NFLs. The 4-u.c. film shows a MIT and recovers LFL behavior. Noninclusion of ρ_{SAT} (*6*, *15*–*18*) would have resulted in the interpretation of the metallic state as an NFL even in the case of an LFL film, with apparent changes in the exponent n for different temperature ranges (Fig. 2A). For example, $n = 1$ is assumed and ρ_{SAT} is neglected for the dashed orange line in Fig. 2A. For the final fits shown in Fig. 1, the exponent n was fixed at 2 or 5/3 (by the closest value). The changes in the results were minimal, but a fixed exponent allows for more reliable comparisons across the series for the slope A (fig. S4).

Figure 2C shows ρ_{SAT} and ρ(0) (metallic resistivity extrapolated to $T = 0$ K, as extracted from the fits) as a function of film thickness. Following Eq. 2

$$\rho^{-1}(0) = \rho_{NFL}^{-1}(0) + \rho_{SAT}^{-1} = \rho_0^{-1} + \rho_{SAT}^{-1}. \quad (4)$$

For most films, $\rho_0 \ll \rho_{SAT}$; thus, $\rho(0) \sim \rho_0$. At low thicknesses, ρ_0 sharply increases, which is the ubiquitously observed rise of resistivity

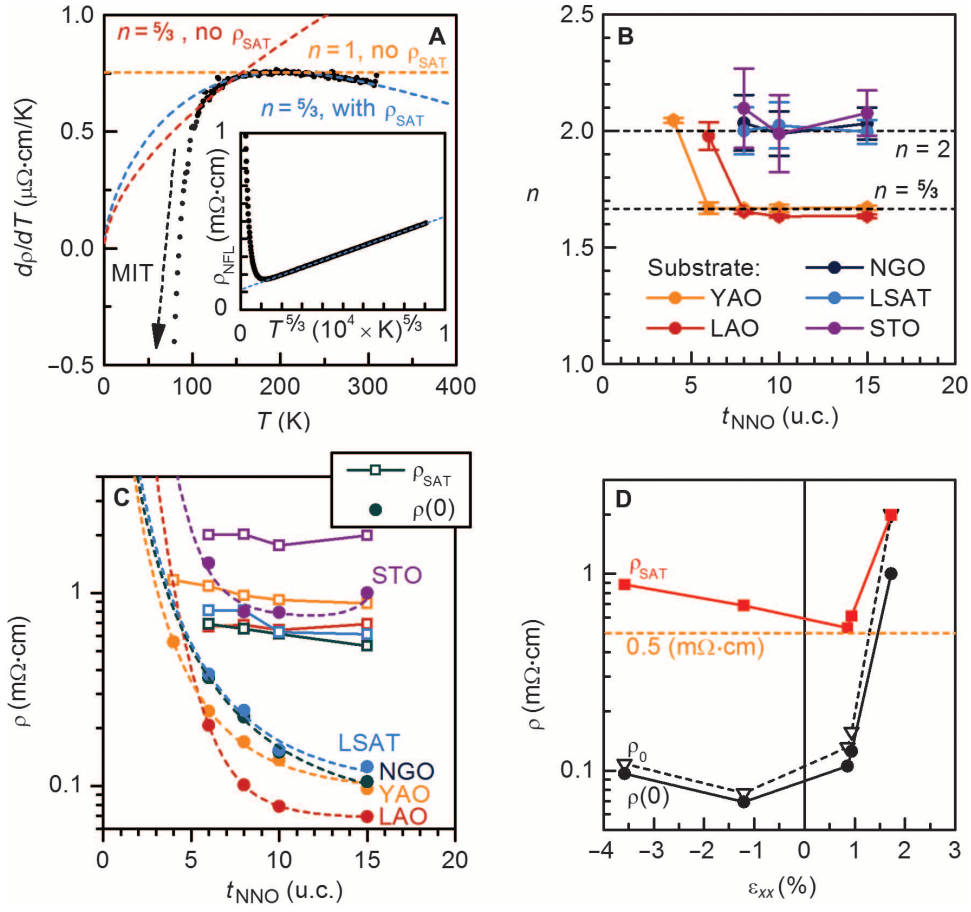

Fig. 2. Resistance saturation and NFL behavior in the metallic state. (**A**) Temperature derivative of the resistivity as a function of temperature (8-u.c. film on $LaAlO_3$). The negative slope at higher temperatures is a manifestation of ρ_{SAT} in Eq. 2, and the dashed blue curve is a fit to Eq. 2 and $n = {}^5/_3$. The downturn at lower temperatures represents the MIT. The red and orange dashed curves are fits to Eq. 1, with $n = {}^5/_3$ and 1, respectively, which cannot describe the data. (Inset) A plot of ρ_{NFL} (extracted from the fit to Eq. 2) as a function of $T^{5/3}$. (**B**) Extracted exponents n for different film thicknesses (t_{NNO}) and substrates [YAO, $YAlO_3$; LAO, $LaAlO_3$; NGO, $NdGaO_3$; LSAT, $(LaAlO_3)_{0.3}(Sr_2AlTaO_6)_{0.7}$; STO, $SrTiO_3$]. (**C**) ρ_{SAT} and $\rho(0)$ as a function of t_{NNO} for the different substrates. Dashed lines are extrapolated polynomial fits to $\rho(0)$ used to determine the thicknesses corresponding to $\rho_{SAT} = \rho(0)$ for the different substrates. (**D**) ρ_{SAT}, ρ_0, and $\rho(0)$ as a function of the in-plane epitaxial strain (ε_{xx}) for the 15-u.c. films. The dashed line represents the Mott-Ioffe-Regel limit according to Eq. 3.

in ultrathin nickelates (*33*–*36*). In contrast, ρ_{SAT} is essentially thickness-independent. ρ_{SAT} does depend, however, on the magnitude of epitaxial strain, as determined by the substrate. This is further illustrated in Fig. 2D, where ρ_{SAT}, ρ_0, and $\rho(0)$ are shown as a function of the in-plane strain ε_{xx} for 15-u.c. films. ρ_{SAT} increases for both compressive and tensile strains. A larger increase is observed on the tensile side, where enhancement by a factor of ~4 is found for the case of a metallic film on $SrTiO_3$. Also shown in Fig. 2D (dashed line) is an estimate of ρ_{MIR} using Eq. 3 with $k_F^3 = 3\pi^2 N$ and a carrier density $N \approx 10^{22}$ cm^{-3}, which gives $\rho_{MIR} \approx 0.5$ mΩ·cm (*8*). Only for small strains is ρ_{SAT} similar to the ρ_{MIR} calculated by this estimate. Analysis of $LaNiO_3$ films (*33*) reveals a ρ_{SAT} as high as 4 mΩ·cm (fig. S3).

The conditions yielding LFL or NFL phases and MITs are summarized in Figs. 3 and 4. Figure 3B shows phase behavior as a function of strain and film thickness (t). We distinguish four types of ρ-T curves (see Fig. 3A for examples): paramagnetic NFL metal at all temperatures [PM(NFL); light blue], an FL metal at high temperatures with a sharp hysteretic transition to an antiferromagnetic Mott insulator near 150 K [PM(FL)↔AFI; yellow], an NFL metal with a strongly suppressed MIT [PM(NFL)↔AFI; dark blue], and insulating behavior at all measured T [AFI; red]. An important feature in Fig. 3 is the pronounced curvature of the transition boundaries. This is a result of similar transport types shifting to lower thickness with increasing compressive strain. For example, the PM(FL)↔AFI region (sharp hysteretic transition, $n = 2$) occurs at $t > 6$ u.c. for tensile strain, at 6 u.c. only for films on $LaAlO_3$, and at 4 u.c. only for films on $YAlO_3$ (largest compressive strain). Similar trends are seen for the occurrence of PM(NFL), PM(NFL)↔I, and the "Anderson insulator" (insulating behavior at all temperatures; red in Fig. 3).

Figure 4 shows the strain-temperature phase diagram. The transition boundaries shown are consistent with Fig. 3. The curvature of the boundaries in Fig. 3 is a result of the lateral shift (parallel to the strain axis) of the entire phase diagram with $NdNiO_3$ film thickness.

DISCUSSION

Tunable bad metal

A key result is that $NdNiO_3$ clearly exhibits resistance saturation in the high-temperature limit. It is thus a bad metal only in the sense that the saturation resistance exceeds the resistance predicted by the Mott-Ioffe-Regel

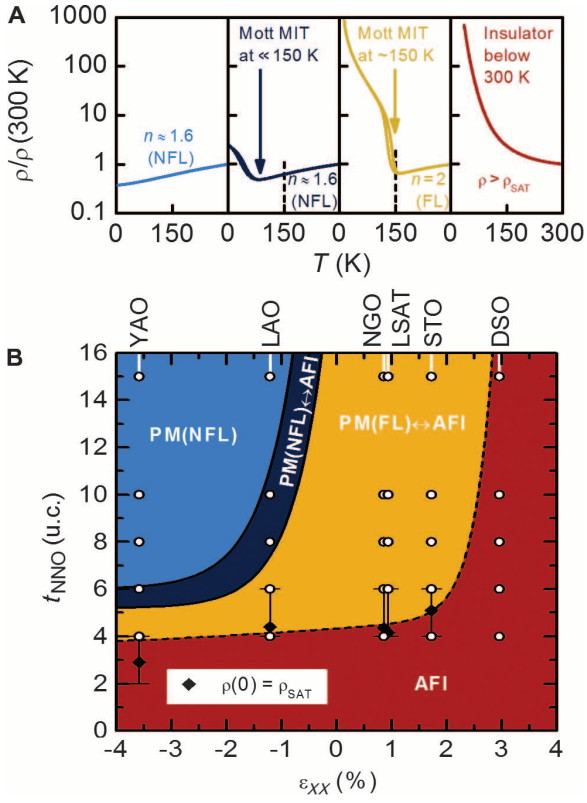

Fig. 3. Strain-thickness phase diagram. (**A**) Prototypes for the four basic behaviors seen in the ρ-*T* curves shown in Fig. 1. (**B**) Phase diagram for ε_{xx} versus t_{NNO}. The boundaries are drawn between the four basic behaviors shown in (A). Each point indicates a transport curve in Fig. 1. Black diamonds represent predictions for MIT based on $\rho(0) = \rho_{SAT}$.

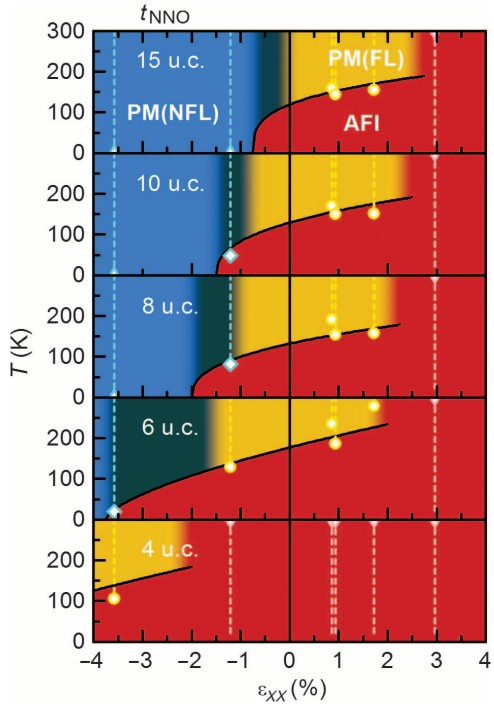

Fig. 4. Strain-temperature phase diagram. Each panel corresponds to a different $NdNiO_3$ (NNO) thickness. Symbols indicate MIT temperatures measured for films under different strains. The colors of the regions correspond to those in Fig. 3, and boundaries are drawn to be consistent with Fig. 3. YAO, $YAlO_3$; LAO, $LaAlO_3$; NGO, $NdGaO_3$; LSAT, $(LaAlO_3)_{0.3}(Sr_2AlTaO_6)_{0.7}$; STO, $SrTiO_3$; DSO, $DyScO_3$.

criterion (Eq. 3), but not in the sense that its resistance escalates without saturation (as in the cuprates). In the following, we discuss the origins of this behavior and its correlation to the electronic structure of this system.

Several theoretical studies have pointed to the importance of orbital degeneracy and specific scattering mechanisms in determining ρ_{SAT} (*30*, *32*). Transport calculations that include interband scattering show that this produces a new conducting channel whose magnitude is proportional within the first order to the interband spacing Δ (*29*, *30*). In this theory, interband currents act as a parallel conducting channel that reduces resistance, leading to a saturating resistance as described by Eq. 2, with $\rho_{SAT} \sim |\Delta|$. The behavior of ρ_{SAT} as a function of strain in $NdNiO_3$ thin films can then be rationalized as a consequence of e_g band splitting. In the rare-earth nickelates, two Ni e_g bands cross the Fermi level. These are derived from orbitals having $x^2 - y^2$ and $3z^2 - r^2$ symmetry, which are degenerate in unstrained bulk material. Experiments have shown that epitaxial strain lifts degeneracy and causes orbital polarization, with tensile strains lowering the energy *E* of $x^2 - y^2$ orbitals and with compressive strains lowering the energy *E* of $3z^2 - r^2$ orbitals (*37*–*39*). Figure 5 shows the magnitude of the orbital splitting $|\Delta| = E(3z^2 - r^2) - E(x^2 - y^2)$ for $NdNiO_3$ as a function of strain, as estimated by density functional theory. With increasing epitaxial strain, orbital polarization increases, in keeping with prior experimental and theoretical findings (*37*–*39*), as does ρ_{SAT}. Moreover, electron-electron scattering strength (*A* in Eq. 1) follows a similar trend with strain as ρ_{SAT} (fig. S4). This trend may also be an indication of the increasing importance of interband scattering, which can lead to resistance from electron-electron scattering, in addition to Umklapp processes (*40*). The strain-tunable ρ_{SAT} allows us to understand how electronic structure determines ρ_{SAT} and thereby (the degree of) bad metal behavior. Specifically, $\rho_{SAT} \propto |\Delta| = E(3z^2 - 1) - E(x^2 - y^2)$ (orbital polarization; inset to Fig. 5B). Thus, a large orbital splitting causes ρ_{SAT} to rise above the value predicted by Eq. 3 (~0.5 mΩ·cm) and the appearance of bad metal behavior (in the sense that ρ exceeds ρ_{MIR}).

Calculations for cuprates predict that these compounds will also saturate [which appears to be confirmed in the experiment (*10*)] but that ρ_{SAT} will be very large because of the fact that only a single $x^2 - y^2$ orbital band crosses the Fermi level (*32*, *41*) (in contrast to the nickelates studied here) and because of strong electron correlations. A large ρ_{SAT} makes the second term in Eq. 2 small and causes a nonsaturating resistance. The experimental results confirm the importance of orbital degeneracy: as we lift degeneracy toward a more cuprate-like Fermi surface with a single band, ρ_{SAT} increases.

Our results also show that although ρ_{SAT} is sensitive to the degree of orbital polarization, it is relatively insensitive to disorder. This can be seen from the very different behaviors of ρ_{SAT} and ρ_0 with decreasing film thickness: ρ_0 sharply increases presumably because of increased scattering by the surface, whereas ρ_{SAT} remains approximately constant (Fig. 2C).

Using the data presented in Fig. 2C, we can make predictions for the occurrence of Anderson localization in this system. In particular, films become insulating at all temperatures when $\rho(0) \approx \rho_{SAT}$; in other

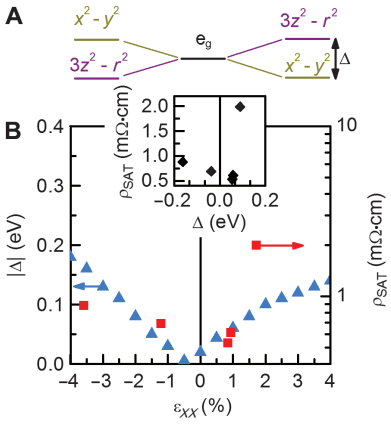

Fig. 5. Saturation resistance and orbital splitting as a function of strain. (**A**) Schematic showing the lifting of e_g orbital degeneracy in $NdNiO_3$. (**B**) Magnitude of the calculated orbital splitting $|\Delta|$ in $NdNiO_3$ and measured ρ_{SAT} as a function of ε_{xx}. (Inset) Correlation between the two quantities.

words, ρ_0 becomes so large that, essentially at all temperatures, the first term in Eq. 2 is smaller than the second term and the resistance is dominated by ρ_{SAT}. Such a material clearly cannot be a metal anymore, and films become insulating at all temperatures. The black diamonds in the phase diagram shown in Fig. 3B are predictions for the critical thickness for this transition, obtained by extrapolating $\rho(0)$ to the point where it intersects with ρ_{SAT}. They agree with the experimental transition within one unit cell. Because ρ_0 contains the effects of disorder, $RNiO_3$ films that are insulating at all temperatures are strongly localized because of disorder, as has also been suggested in the literature (*33*, *34*, *42*). We loosely term this the Anderson insulator, although correlations presumably play a role and the insulator may be magnetic (*43*). The criterion [$\rho(0) \approx \rho_{SAT}$] established here has an interesting implication, namely, that the Anderson insulating state is tunable in a similar fashion as ρ_{SAT}. Specifically, materials with a large ρ_{SAT} will require larger ρ_0 values to become insulating and can be considered as more disorder-tolerant, all other things being equal. Unlike A and ρ_{SAT}, however, ρ_0 does depend on the sign of the strain and not only on its magnitude. This is attributable to ρ_0 being a function of the size of the Fermi surface (*44*), which changes with strain (*38*). Tensile strained films, with their larger ρ_0, fulfill $\rho(0) \approx \rho_{SAT}$ at larger thicknesses than compressively strained films (see data on $SrTiO_3$ in Fig. 2C).

NFL behavior

The phase diagrams shown in Figs. 3 and 4 illustrate the two distinct types of MITs: the quantum phase transition at 0 K between an NFL and an antiferromagnetic insulator (blue-yellow crossover) and the disorder-driven transition to the Anderson insulator (yellow-red crossover), when $\rho(0) \approx \rho_{SAT}$. The quantum phase transition as a function of strain has been documented in relatively thick $RNiO_3$ films (*6*, *45*–*47*). The nature of this MIT—as being driven by Fermi surface nesting and spin density wave (promoting the insulating state) (*38*, *43*, *48*, *49*) or in terms of bandwidth and charge-transfer energy (*6*, *45*, *50*)—has been extensively discussed in the literature. The insulating phase at low thicknesses has also been linked to the stabilization of the spin density wave order, acting similarly to tensile strain (*37*, *38*). This work establishes that the location of the quantum phase transition is highly sensitive to both strain and confinement. This is reflected in the curved phase boundaries in Fig. 3 and, equivalently, in the continuous shift of the entire phase diagram toward compressive strain at low thickness in Fig. 4. Moreover, at high tensile strains, the Mott MIT and the disorder-driven Anderson transition are brought in increasingly close proximity to each other. The dual nature of the driving mechanisms promoting the insulating transition should be an important consideration in interpreting phenomena such as magnetism (*34*). The two transitions can be decoupled using strain (for example, as in $NdNiO_3$ grown on $LaAlO_3$).

The results have further intriguing implications for the nature of NFL-LFL crossover in the metallic phase, which is abrupt and coincides with the suppression of the temperature-driven MIT. The exponent n is insensitive to disorder, which increases (according to ρ_0) with decreasing film thickness (Fig. 2, B and C). This is contrary to the expectations of NFL behavior driven by spin fluctuations, which should yield n values that are highly sensitive to disorder (*51*). Furthermore, it is constant across all of the NFL phases observed here. $n \approx 5/3$ has also been observed for $PrNiO_3$ and $EuNiO_3$ under pressure when the temperature-driven MIT is suppressed (*52*, *53*), as well as in overdoped cuprates (*54*, *55*). This points to a common origin that requires further theoretical investigations. Specifically, future studies should address the question of whether a quantum critical point or a distinct NFL phase is the origin of NFL metal. Our results emphasize the need for a quantitative treatment of electronic structure and, in keeping with earlier suggestions (*4*, *5*), that nickelates are a fertile ground to investigate aspects of the normal states of cuprates.

Applications

The phase diagram presented in Fig. 3 can be used as a guide in designing future devices based on controlling the MIT of nickelates. The M(NFL)↔I pocket at compressive strains and low film thicknesses could be useful for electrostatic control (*56*–*60*), which requires thin films to make carrier density modulation feasible while still permitting a sharp MIT with many orders of magnitude of resistance change. Strain control of MIT may also be of interest for low-voltage digital switches (*61*). On the tensile side of the phase diagram, the sharp M(NFL)↔I/I boundary is noteworthy because a small amount of strain, controlled by a piezoelectric material, can have a large effect on resistivity at temperatures relevant to practical devices. In particular, Fig. 3 shows a strain-tunable transition between the Anderson insulator [$\rho(0) = \rho_{SAT}$] and the Mott MIT.

MATERIALS AND METHODS

Films were grown by radio frequency magnetron sputtering in a 95% Ar/5% O_2 mixture, a total pressure of 9 mTorr, and a sputter power of 15 W. The optimization of growth conditions, the structure and chemical composition of films, and the quantification of mismatch strains have been reported elsewhere (*47*). Methods used to characterize the films included high-resolution x-ray diffraction, scanning transmission electron microscopy, and Rutherford backscattering spectrometry, as described by Hauser *et al.* (*47*). Films of a given thickness were simultaneously deposited on different substrates. The magnitude of the in-plane strain was calculated as $\varepsilon_{xx} = (a_{\parallel} - a_0)/a_0$, where $a_{\parallel}$ is the measured in-plane lattice constant and a_0 is the unstrained (intrinsic) lattice parameter, which was extracted from x-ray diffraction as described by Hauser *et al.* (*47*). Resistivity was determined from measurements in a van der Pauw configuration with $Ni_{20\ nm}/Au_{300\ nm}$ ohmic contacts

(between 2 and 300 K) using the Physical Properties Measurement System (Quantum Design Inc.).

Electronic structure calculations were performed using projector-augmented wave formalism (*62*), as implemented in the QUANTUM ESPRESSO package (*63*). Electronic wave functions were expanded up to a kinetic energy cutoff of 50 Ry. Brillouin zone integrations were performed on a 8 × 8 × 8 special *k*-point grid and using Methfessel-Paxton smearing (*64*) of the Fermi-Dirac distribution function with a smearing width of 0.01 Ry. We used the generalized gradient approximation for the exchange correlation functional [Perdew-Burke-Ernzerhof (PBE)] (*65*). The crystal structure was constrained to a tetragonal unit cell with the *ab* plane fixed to the lattice constant of the substrate, whereas the *c* lattice parameter was allowed to relax. For the calculation of crystal field splittings, we constructed maximally localized Wannier functions (*66*) and a real-space Hamiltonian in Wannier function basis. The splitting between the diagonal elements of the real-space Hamiltonian of the e_g-like Wannier functions for different strain configurations was interpreted as crystal-field splitting for the e_g states, defined as $\Delta = H(z^2,z^2) - H(x^2 - y^2, x^2 - y^2)$, with H representing the real-space Hamiltonian in Wannier function basis. Although the PBE functional and the tetragonal unit cell did not reproduce the insulating and E'-type antiferromagnetic ordering of bulk $NdNiO_3$, they provided the correct qualitative behavior and trends for the dependence of Δ as a function of strain. In addition, we expected the metallic solution to provide a better description of the electronic properties of metallic $NdNiO_3$ films, compared to those of bulk $NdNiO_3$, within the PBE functional.

SUPPLEMENTARY MATERIALS

Supplementary material for this article is available at http://advances.sciencemag.org/cgi/content/full/1/10/1500797/DC1

Fig. S1. Resistivity as a function of temperature.

Fig. S2. ρ-*T* data for $LaNiO_3$.

Fig. S3. Saturation resistivity and NFL behavior in $LaNiO_3$.

Fig. S4. Electron-electron scattering coefficient *A*.

REFERENCES AND NOTES

1. P. A. Lee, N. Nagaosa, X.-G. Wen, Doping a Mott insulator: Physics of high-temperature superconductivity. *Rev. Mod. Phys.* **78**, 17–85 (2006).
2. J. B. Torrance, P. Lacorre, A. I. Nazzal, E. J. Ansaldo, Ch. Niedermayer, Systematic study of insulator-metal transitions in perovskites $RNiO_3$ (*R* = Pr,Nd,Sm,Eu) due to closing of charge-transfer gap. *Phys. Rev. B Condens. Matter* **45**, 8209–8212 (1992).
3. M. L. Medarde, Structural, magnetic and electronic properties of $RNiO_3$ perovskites (R = rare earth). *J. Phys. Condens. Matter* **9**, 1679–1707 (1997).
4. J. Chaloupka, G. Khaliullin, Orbital order and possible superconductivity in $LaNiO_3/LaMO_3$ superlattices. *Phys. Rev. Lett.* **100**, 016404 (2008).
5. P. Hansmann, X. Yang, A. Toschi, G. Khaliullin, O. K. Andersen, K. Held, Turning a nickelate Fermi surface into a cupratelike one through heterostructuring. *Phys. Rev. Lett.* **103**, 016401 (2009).
6. J. Liu, M. Kargarian, M. Kareev, B. Gray, P. J. Ryan, A. Cruz, N. Tahir, Y.-D. Chuang, J. Guo, J. M. Rondinelli, J. W. Freeland, G. A. Fiete, J. Chakhalian, Heterointerface engineered electronic and magnetic phases of $NdNiO_3$ thin films. *Nat. Commun.* **4**, 2714 (2013).
7. S. J. Allen, A. J. Hauser, E. Mikheev, J. Y. Zhang, N. E. Moreno, J. Son, D. G. Ouellette, J. Kally, A. Kozhanov, L. Balents, S. Stemmer, Gaps and pseudogaps in perovskite rare earth nickelates. *APL Mater.* **3**, 062503 (2015).
8. R. Jaramillo, S. D. Ha, D. M. Silevitch, S. Ramanathan, Origins of bad-metal conductivity and the insulator–metal transition in the rare-earth nickelates. *Nat. Phys.* **10**, 304–307 (2014).
9. V. J. Emery, S. A. Kivelson, Superconductivity in bad metals. *Phys. Rev. Lett.* **74**, 3253–3256 (1995).
10. N. E. Hussey, K. Takenaka, H. Takagi, Universality of the Mott–Ioffe–Regel limit in metals. *Philos. Mag.* **84**, 2847–2864 (2004).
11. P. B. Allen, Condensed-matter physics: Misbehaviour in metals. *Nature* **405**, 1007–1008 (2000).
12. P. B. Allen, Metals with small electron mean-free path: Saturation versus escalation of resistivity. *Phys. B Condens. Matter* **318**, 24–27 (2002).
13. A. J. Millis, J. Hu, S. D. Sarma, Resistivity saturation revisited: Results from a dynamical mean field theory. *Phys. Rev. Lett.* **82**, 2354–2357 (1999).
14. O. Gunnarsson, J. E. Han, The mean free path for electron conduction in metallic fullerenes. *Nature* **405**, 1027–1030 (2000).
15. X. Q. Xu, J. L. Peng, Z. Y. Li, H. L. Ju, R. L. Greene, Resisitivity, thermopower, and susceptibility of $RNiO_3$ (*R* = La,Pr). *Phys. Rev. B Condens. Matter* **48**, 1112–1118 (1993).
16. J. Blasco, J. Garcia, A comparative study of the crystallographic, magnetic and electrical properties of the $Nd_{1-x}La_xNiO_{3-delta}$ system. *J. Phys. Condens. Matter* **6**, 10759–10772 (1994).
17. N. Gayathri, A. K. Raychaudhuri, X. Q. Xu, J. L. Peng, R. L. Greene, Electronic conduction in $LaNiO_{3-\delta}$: The dependence on the oxygen stoichiometry δ. *J. Phys. Condens. Matter* **10**, 1323–1338 (1998).
18. E. J. Moon, B. A. Gray, M. Kareev, J. Liu, S. G. Altendorf, F. Strigari, L. H. Tjeng, J. W. Freeland, J. Chakhalian, Strain-dependent transport properties of the ultra-thin correlated metal, $LaNiO_3$. *New J. Phys.* **13**, 073037 (2011).
19. H. Wei, M. Jenderka, M. Bonholzer, M. Grundmann, M. Lorenz, Modeling the conductivity around the dimensionality-controlled metal-insulator transition in $LaNiO_3/LaAlO_3$ (100) superlattices. *Appl. Phys. Lett.* **106**, 042103 (2015).
20. N. E. Hussey, Phenomenology of the normal state in-plane transport properties of high-T_c cuprates. *J. Phys. Condens. Matter* **20**, 123201 (2008).
21. H. Wiesmann, M. Gurvitch, H. Lutz, A. Ghosh, B. Schwarz, M. Strongin, P. B. Allen, J. W. Halley, Simple model for characterizing the electrical resistivity in *A* − 15 superconductors. *Phys. Rev. Lett.* **38**, 782–785 (1977).
22. R. Caton, R. Viswanathan, Analysis of the normal-state resistivity for the neutron-irradiated A15 superconductors V_3Si, Nb_3Pt, and Nb_3Al. *Phys. Rev. B* **25**, 179–193 (1982).
23. A. de Visser, J. J. M. Franse, A. Menovsky, Resistivity of single-crystalline UPt_3 and its pressure dependence; Interpretation by a spin-fluctuation model. *J. Magn. Magn. Mater.* **43**, 43–47 (1984).
24. H. M. Milchberg, R. R. Freeman, S. C. Davey, R. M. More, Resistivity of a simple metal from room temperature to 10^6 K. *Phys. Rev. Lett.* **61**, 2364–2367 (1988).
25. B. Sundqvist, Resistivity saturation in fcc La under high pressure. *Phys. Rev. Lett.* **69**, 2693–2696 (1992).
26. T. K. Nath, A. K. Majumdar, Resistivity saturation in substitutionally disordered γ-$Fe_{80-x}Ni_xCr_{20}$ ($14 \leq x 30$) alloys. *Phys. Rev. B Condens. Matter* **53**, 12148–12159 (1996).
27. O. Gunnarsson, M. Calandra, J. E. Han, Colloquium: Saturation of electrical resistivity. *Rev. Mod. Phys.* **75**, 1085–1099 (2003).
28. M. Gurvitch, Ioffe-Regel criterion and resistivity of metals. *Phys. Rev. B Condens. Matter* **24**, 7404–7407 (1981).
29. P. B. Allen, in *Superconductivity in D- and F-Band Metals*, H. Suhl, M. B. Maple, Eds. (Academic Press, New York, 1980), pp. 291–304.
30. B. Chakraborty, P. B. Allen, Boltzmann theory generalized to include band mixing: A possible theory for "resistivity saturation" in metals. *Phys. Rev. Lett.* **42**, 736–738 (1979).
31. R. A. Cooper, Y. Wang, B. Vignolle, O. J. Lipscombe, S. M. Hayden, Y. Tanabe, T. Adachi, Y. Koike, M. Nohara, H. Takagi, C. Proust, N. E. Hussey, Anomalous criticality in the electrical resistivity of $La_{2-x}Sr_xCuO_4$. *Science* **323**, 603–607 (2009).
32. M. Calandra, O. Gunnarsson, Electrical resistivity at large temperatures: Saturation and lack thereof. *Phys. Rev. B Condens. Matter* **66**, 205105 (2002).
33. J. Son, P. Moetakef, J. M. LeBeau, D. Ouellette, L. Balents, S. J. Allen, S. Stemmer, Low-dimensional Mott material: Transport in ultrathin epitaxial $LaNiO_3$ films. *Appl. Phys. Lett.* **96**, 062114 (2010).
34. R. Scherwitzl, S. Gariglio, M. Gabay, P. Zubko, M. Gibert, J. M. Triscone, Metal-insulator transition in ultrathin $LaNiO_3$ films. *Phys. Rev. Lett.* **106**, 246403 (2011).
35. P. D. C. King, H. I. Wei, Y. F. Nie, M. Uchida, C. Adamo, S. Zhu, X. He, I. Božović, D. G. Schlom, K. M. Shen, Atomic-scale control of competing electronic phases in ultrathin $LaNiO_3$. *Nat. Nanotechnol.* **9**, 443–447 (2014).
36. A. V. Boris, Y. Matiks, E. Benckiser, A. Frano, P. Popovich, V. Hinkov, P. Wochner, M. Castro-Colin, E. Detemple, V. K. Malik, C. Bernhard, T. Prokscha, A. Suter, Z. Salman, E. Morenzoni, G. Cristiani, H.-U. Habermeier, B. Keimer, Dimensionality control of electronic phase transitions in nickel-oxide superlattices. *Science* **332**, 937–940 (2011).
37. M. Wu, E. Benckiser, M. W. Haverkort, A. Frano, Y. Lu, U. Nwankwo, S. Brück, P. Audehm, E. Goering, S. Macke, V. Hinkov, P. Wochner, G. Christiani, S. Heinze, G. Logvenov, H.-U. Habermeier, B. Keimer, Strain and composition dependence of orbital polarization in nickel oxide superlattices. *Phys. Rev. B* **88**, 125124 (2013).
38. H. K. Yoo, S. I. Hyun, L. Moreschini, H.-D. Kim, Y. J. Chang, C. H. Sohn, D. W. Jeong, S. Sinn, Y. S. Kim, A. Bostwick, E. Rotenberg, J. H. Shim, T. W. Noh, Latent instabilities in metallic $LaNiO_3$ films by strain control of Fermi-surface topology. *Sci. Rep.* **5**, 8746 (2014).
39. O. E. Peil, M. Ferrero, A. Georges, Orbital polarization in strained $LaNiO_3$: Structural distortions and correlation effects. *Phys. Rev. B Condens. Matter* **90**, 045128 (2014).
40. J. Appel, Interband electron-electron scattering and transport phenomena in semiconductors. *Phys. Rev.* **125**, 1815–1823 (1962).

41. M. Calandra, O. Gunnarsson, Violation of Ioffe-Regel condition but saturation of resistivity of the high-T_c cuprates. *Europhys. Lett.* **61**, 88–94 (2003).
42. H. K. Yoo, S. I. Hyun, L. Moreschini, Y. J. Chang, D. W. Jeong, C. H. Sohn, Y. S. Kim, H.-D. Kim, A. Bostwick, E. Rotenberg, J. H. Shim, T. W. Noh, Dimensional crossover of the electronic structure in $LaNiO_3$ ultrathin films: Orbital reconstruction, Fermi surface nesting, and the origin of the metal-insulator transition. (2013) arXiv:1309.0710 [cond-mat.str-el].
43. A. Frano, E. Schierle, M. W. Haverkort, Y. Lu, M. Wu, S. Blanco-Canosa, U. Nwankwo, A. V. Boris, P. Wochner, G. Cristiani, H. U. Habermeier, G. Logvenov, V. Hinkov, E. Benckiser, E. Weschke, B. Keimer, Orbital control of noncollinear magnetic order in nickel oxide heterostructures. *Phys. Rev. Lett.* **111**, 106804 (2013).
44. T. M. Rice, W. F. Brinkman, Effects of impurities on the metal-insulator transition. *Phys. Rev. B Condens. Matter* **5**, 4350–4357 (1972).
45. D. Meyers, E. J. Moon, M. Kareev, I. C. Tung, B. A. Gray, J. Liu, M. J. Bedzyk, J. W. Freeland, J. Chakhalian, Epitaxial stabilization of ultra-thin films of $EuNiO_3$. *J. Phys. D Appl. Phys.* **46**, 385303 (2013).
46. S. Catalano, M. Gibert, V. Bisogni, O. E. Peil, F. He, R. Sutarto, M. Viret, P. Zubko, R. Scherwitzl, A. Georges, G. A. Sawatzky, T. Schmitt, J.-M. Triscone, Electronic transitions in strained $SmNiO_3$ thin films. *APL Mater.* **2**, 116110 (2014).
47. A. J. Hauser, E. Mikheev, N. E. Moreno, J. Hwang, J. Y. Zhang, S. Stemmer, Correlation between stoichiometry, strain, and metal-insulator transitions of $NdNiO_3$ films. *Appl. Phys. Lett.* **106**, 092104 (2015).
48. S. Lee, R. Chen, L. Balents, Landau theory of charge and spin ordering in the nickelates. *Phys. Rev. Lett.* **106**, 016405 (2011).
49. S. Lee, R. Chen, L. Balents, Metal-insulator transition in a two-band model for the perovskite nickelates. *Phys. Rev. B Condens. Matter* **84**, 165119 (2011).
50. B. Lau, A. J. Millis, Theory of the magnetic and metal-insulator transitions in $RNiO_3$ bulk and layered structures. *Phys. Rev. Lett.* **110**, 126404 (2013).
51. A. Rosch, Interplay of disorder and spin fluctuations in the resistivity near a quantum critical point. *Phys. Rev. Lett.* **82**, 4280–4283 (1999).
52. J. S. Zhou, J. B. Goodenough, B. Dabrowski, Pressure-induced non-Fermi-liquid behavior of $PrNiO_3$. *Phys. Rev. Lett.* **94**, 226602 (2005).
53. H. Kobayashi, S. Ikeda, Y. Yoda, N. Hirao, Y. Ohishi, J. A. Alonso, M. J. Martinez-Lope, R. Lengsdorf, D. I. Khomskii, M. M. Abd-Elmeguid, Pressure-induced unusual metallic state in $EuNiO_3$. *Phys. Rev. B* **91**, 195148 (2015).
54. S. Nakamae, K. Behnia, N. Mangkorntong, M. Nohara, H. Takagi, S. J. C. Yates, N. E. Hussey, Electronic ground state of heavily overdoped nonsuperconducting $La_{2-x}Sr_xCuO_4$. *Phys. Rev. B* **68**, 100502(R) (2003).
55. K. Jin, N. P. Butch, K. Kirshenbaum, J. Paglione, R. L. Greene, Link between spin fluctuations and electron pairing in copper oxide superconductors. *Nature* **476**, 73–75 (2011).
56. R. Scherwitzl, P. Zubko, I. G. Lezama, S. Ono, A. F. Morpurgo, G. Catalan, J.-M. Triscone, Electric-field control of the metal-insulator transition in ultrathin $NdNiO_3$ films. *Adv. Mater.* **22**, 5517–5520 (2010).
57. J. Son, B. Jalan, A. P. Kajdos, L. Balents, S. J. Allen, S. Stemmer, Probing the metal-insulator transition of $NdNiO_3$ by electrostatic doping. *Appl. Phys. Lett.* **99**, 192107 (2011).
58. J. Son, S. Rajan, S. Stemmer, S. J. Allen, A heterojunction modulation-doped Mott transistor. *J. Appl. Phys.* **110**, 084503 (2011).
59. S. Asanuma, P.-H. Xiang, H. Yamada, H. Sato, I. H. Inoue, H. Akoh, A. Sawa, K. Ueno, H. Shimotani, H. Yuan, M. Kawasaki, Y. Iwasa, Tuning of the metal-insulator transition in electrolyte-gated $NdNiO_3$ thin films. *Appl. Phys. Lett.* **97**, 142110 (2010).
60. S. Bubel, A. J. Hauser, A. M. Glaudell, T. E. Mates, S. Stemmer, M. L. Chabinyc, The electrochemical impact on electrostatic modulation of the metal-insulator transition in nickelates. *Appl. Phys. Lett.* **106**, 122102 (2015).
61. D. Newns, B. Elmegreen, X. H. Liu, G. Martyna, A low-voltage high-speed electronic switch based on piezoelectric transduction. *J. Appl. Phys.* **111**, 084509 (2012).
62. P. E. Blöchl, Projector augmented-wave method. *Phys. Rev. B Condens. Matter* **50**, 17953–17979 (1994).
63. P. Giannozzi, S. Baroni, N. Bonini, M. Calandra, R. Car, C. Cavazzoni, D. Ceresoli, G. L. Chiarotti, M. Cococcioni, I. Dabo, A. D. Corso, S. de Gironcoli, S. Fabris, G. Fratesi, R. Gebauer, U. Gerstmann, C. Gougoussis, A. Kokalj, M. Lazzeri, L. Martin-Samos, N. Marzari, F. Mauri, R. Mazzarello, S. Paolini, A. Pasquarello, L. Paulatto, C. Sbraccia, S. Scandolo, G. Sclauzero, A. P. Seitsonen, A. Smogunov, P. Umari, R. M. Wentzcovitch, QUANTUM ESPRESSO: A modular and open-source software project for quantum simulations of materials. *J. Phys. Condens. Matter* **21**, 395502 (2009).
64. M. Methfessel, A. T. Paxton, High-precision sampling for Brillouin-zone integration in metals. *Phys. Rev. B Condens. Matter* **40**, 3616–3621 (1989).
65. J. P. Perdew, K. Burke, M. Ernzerhof, Generalized gradient approximation made simple. *Phys. Rev. Lett.* **77**, 3865 (1996).
66. A. A. Mostofi, J. R. Yates, Y.-S. Lee, I. Souza, D. Vanderbilt, N. Marzari, A tool for obtaining maximally-localised Wannier functions. *Comput. Phys. Commun.* **178**, 685–699 (2008).

Acknowledgments: We gratefully acknowledge J. Allen for helpful discussions and for critically reading the manuscript and J. Son for the $LaNiO_3$ data. We also thank L. Balents for discussions. **Funding:** This work was supported in part by FAME, one of the six centers of STARnet, a Semiconductor Research Corp. program sponsored by Microelectronics Advanced Research Corp. and Defense Advanced Research Projects Agency and by the U.S. Army Research Office (grants W911-NF-09-1-0398, W911NF-14-1-0379, and W911-NF-11-1-0232). B.H. was supported by the Office of Naval Research (grant N00014-12-1-0976). A.J.H. was supported through an Elings Prize Fellowship of the California Nanosystems Institute at University of California, Santa Barbara (UCSB). This work used the central facilities of the UCSB Materials Research Laboratory, which was supported by the Materials Research Science and Engineering Centers Program of the NSF (award DMR-1121053). This work also used the UCSB Nanofabrication Facility, a part of the NSF-funded National Nanotechnology Infrastructure Network. **Author contributions:** E.M., N.E.M., and A.J.H. performed film growth and electrical measurements. E.M. analyzed the data. B.H. and A.J. carried out electronic structure calculations. E.M. and S.S. wrote the manuscript. All authors commented on the manuscript. **Competing interests:** The authors declare that they have no competing interests. **Data and materials availability:** All data needed to evaluate the conclusions in the paper are present in the paper and/or the Supplementary Materials. Additional data related to this paper may be requested from the authors.

Submitted 16 June 2015
Accepted 28 August 2015
Published 6 November 2015
10.1126/sciadv.1500797

Citation: E. Mikheev, A. J. Hauser, B. Himmetoglu, N. E. Moreno, A. Janotti, C. G. Van de Walle, S. Stemmer, Tuning bad metal and non-Fermi liquid behavior in a Mott material: Rare-earth nickelate thin films. *Sci. Adv.* **1**, e1500797 (2015).